scientific reports

Check for updates

OPEN

Investigation of structural elastic electronic optical and thermoelectric properties of $LiInS_2$ and $LiInTe_2$ for optoelectronic and energy conversion

M. Fatmi[1]✉, K. Bouferrache[1,2], M. A. Ghebouli[1,3], B. Ghebouli[4], S. Alomairy[5] & Faisal Katib Alanazi[6]

In this research, the structural, electronic, optical, and thermoelectric properties of $LiInX_2$ (X = S, Te) compounds were investigated using first-principles calculations based on Density Functional Theory (DFT). The Full-Potential Linearized Augmented Plane Wave (FP-LAPW) method implemented in the Wien2k package was employed, with the Generalized Gradient Approximation (GGA) and Tran-Blaha modified Becke-Johnson (mBJ-GGA) approximation applied to study the electronic properties. The results revealed that $LiInS_2$ crystallizes in an orthorhombic system with space group Pna21, while $LiInTe_2$ crystallizes in a tetragonal system with space group I-42d. The lattice constants and elastic parameters were calculated, showing good agreement with available experimental values. The elastic properties, including elastic constants, moduli, and mechanical stability criteria, were also evaluated to provide insight into the structural robustness and potential mechanical performance of the compounds. Electronic band structure calculations revealed that both compounds possess direct band gaps, with values of 3.61 eV for $LiInS_2$ and 2.33 eV for $LiInTe_2$ using the mBJ-GGA approximation, which are close to experimental measurements. Phonon dispersion studies were conducted to verify the dynamic stability of both compounds. Our findings demonstrate that $LiInX_2$ (X = S, Te) compounds possess suitable electronic band structures, strong optical absorption in the visible and UV ranges, and favorable thermoelectric characteristics. These results highlight their potential as promising materials for both optoelectronic devices and thermoelectric energy conversion technologies.

Keywords $LiInS_2$, $LiInTe_2$, Optical properties, Thermoelectric properties, Phonon, Optoelectronic applications

Ternary I-III-VI_2 semiconductor compounds have attracted significant attention in scientific research and technological applications due to their distinctive physical and chemical properties[1–3]. Among these compounds, $LiInX_2$ (X = S, Te) are of particular interest because of their excellent nonlinear optical properties and potential applications in optoelectronic devices, solar cells, and thermoelectric energy conversion devices[4–6]. $LiInS_2$ is a wide-band-gap semiconductor characterized by high transparency in the visible and near-infrared regions of the electromagnetic spectrum[7]. It has been proposed for various applications such as tunable lasers, second harmonic generators, and energy converters[8]. On the other hand, $LiInTe_2$ has been less studied but shows promising properties for optical devices and energy conversion applications[9]. Despite some experimental studies on these compounds, the understanding of their fundamental properties at the theoretical level remains limited. In this context, first-principles calculations based on density functional theory (DFT) provide a powerful tool

[1]Research Unit on Emerging Materials (RUEM), University Ferhat Abbas of Setif 1, Setif 19000, Algeria. [2]Department of Physics, Faculty of Science, University of M'sila University Pole, Road Bourdj Bou Arreiridj, 28000 M'sila, Algeria. [3]Department of Chemistry, Faculty of Sciences, University of M'sila University Pole, Road Bourdj Bou Arreiridj, 28000 M'sila, Algeria. [4]Laboratory of Studies Surfaces and Interfaces of Solids Materials, Department of Physics, Faculty of Science, University Ferhat Abbas of Setif 1, Sétif 19000, Algeria. [5]Department of Physics, College of Science, Taif University, Taif 21944, Saudi Arabia. [6]Department of Physics, college of Sciences, Northern Border University, Arar 73222, Saudi Arabia. ✉email: fatmimessaoud@yahoo.fr

for systematically and accurately studying the physical properties of these materials[10]. Recently, Karaagac et al. (2023) investigated the structural, electronic, and optical properties of $LiInSe_2$ compounds using the FP-LAPW method and revealed their high potential for photovoltaic applications[11]. Wang et al. (2022) conducted a comparative study of the thermoelectric properties of several I-III-VI_2 compounds and showed that these materials could be promising candidates for thermoelectric energy conversion applications[12]. Recent studies have revealed increasing potential for $LiInX_2$ compounds in a variety of technological applications. Sharma et al. (2024) investigated the defect-induced enhancement of thermoelectric properties in $LiInS_2$, suggesting the possibility of improving the performance of these materials through defect concentration control[13]. Zhang et al. (2023) proposed the possibility of band gap engineering in $LiInX_2$ (X = S, Se, Te) compounds via strain and doping, opening new horizons for semiconductor applications[14]. In the field of renewable energy applications, Chen et al. (2024) demonstrated the potential of solution-processed $LiInS_2$ thin films for next-generation transparent photovoltaics[15]. Zhou et al. (2023) revealed emergent ferroelectricity in chalcopyrite $LiInX_2$ structures under pressure, expanding the range of potential applications for these materials[16]. Regarding the less-studied $LiInTe_2$ compound, Lee et al. (2023) analyzed structural phase transitions under hydrostatic pressure using first-principles calculations[17]. Additionally, Wang et al. (2024) developed high-performance flexible photodetectors based on $LiInS_2$ nanocrystals with enhanced stability[18]. The field of discovery of new $LiInX_2$-based materials is rapidly evolving with the use of advanced techniques. Mehta et al. (2023) utilized machine learning techniques for the discovery of novel $LiInX_2$-based materials for optoelectronic applications[19]. Ortiz-Ramos et al. (2024) conducted a comparative study of electronic and optical properties of $LiInX_2$ (X = S, Se, Te) compounds using hybrid functionals, providing deeper understanding of their physical behavior[20]. Lin et al. (2023) revealed new insights into the electronic structure and optical properties of $LiInTe_2$ through GW calculations and experimental measurements[21]. Finally, Ahmad et al. (2024) explored the potential of $LiInS_2$ for high-efficiency all-solid-state batteries using a multiscale modeling approach, opening a potential new field for applications of these compounds[22]. Based on previous studies, there is a need for a deeper understanding of the physical properties of $LiInX_2$ (X = S, Te) compounds, particularly regarding optical and thermoelectric properties that have not received sufficient attention in previous research. Therefore, this research aims to conduct a comprehensive study of the structural, electronic, optical, and thermoelectric properties of these compounds using first-principles calculations. In this work, we systematically investigate the structural, electronic, and phonon properties of $LiInX_2$ (X = S, Te) using first-principles calculations. We also compute a complete set of optical properties, including the real and imaginary parts of the dielectric function, refractive index, absorption coefficient, reflectivity, and optical conductivity. Furthermore, we evaluate key thermoelectric parameters such as the Seebeck coefficient, electrical and thermal conductivity, power factor, and the dimensionless figure of merit (ZT) over a wide temperature range. These results offer comprehensive insight into the multifunctional behavior of these compounds. The results of this study are expected to guide experimental efforts toward developing practical applications of these compounds in optoelectronic and energy conversion fields. This work presents, for the first time, a comprehensive theoretical investigation of $LiInX_2$ (X = S, Te) compounds, combining structural, electronic, optical, phonon, and thermoelectric analyses within a unified DFT framework. Unlike earlier reports that focused only on selected properties, our study provides a complete picture of the material behavior, highlighting their potential as multifunctional materials for optoelectronic and thermoelectric technologies.

Computational methods

The WIEN2k code was chosen due to its full-potential all-electron approach, based on the FP-LAPW + lo method[23]., which offers highly accurate results for the electronic structure of complex materials. Its robustness in computing both the band structure and optical spectra with high precision made it the ideal tool for this investigation. This method is based on Density Functional Theory (DFT) and is considered one of the most accurate methods for calculating the electronic properties of solid materials. The Generalized Gradient Approximation (GGA) proposed by Perdew-Burke-Ernzerhof (PBE)[24] was used to describe the exchange-correlation energy in calculations for structural optimization and the determination of structural and mechanical properties. To improve the description of the band gap and electronic properties, the Tran-Blaha modified Becke-Johnson (mBJ-GGA) approximation[25] was employed, which has proven effective in predicting band gap values more accurately compared to conventional DFT approximations. The crystalline space was divided into two regions: spherically symmetric muffin-tin (MT) regions around atomic sites and an interstitial region. The muffin-tin radii were chosen to be 2.12, 2.50, and 2.09 Bohr for Li, In, and S elements, respectively, and 2.12, 2.50, and 2.50 Bohr for Li, In, and Te elements, respectively, as shown in Table 1. The $R_{MT} \times K_{max}$ value was set to 9, where RMT is the smallest muffin-tin radius and Kmax is the maximum value of the wave vector in the plane wave expansion. Different k-point meshes were used depending on the nature of the calculation. A $10 \times 10 \times 10$ grid was employed for structural optimization to achieve energy convergence. For electronic and optical properties, a denser $12 \times 12 \times 12$ mesh was utilized to capture finer details in the band structure. Thermoelectric calculations, performed using the BoltzTraP code, required a much denser mesh (up to $20 \times 20 \times 20$) to ensure accuracy in the energy derivatives needed for transport coefficients. A convergence criterion of 10^{-5} Ry for

	$R_{MT}.K_{max}$	R_{MT}(Li)	R_{MT}(In)	R_{MT}(X)
$LiInS_2$	9	2.12	2.50	2.09
$LiInTe_2$	9	2.12	2.50	2.50

Table 1. Using GGA, the values of rmtxkmax, RMT for each component, and k-point $LiInX_2$ (X = S, Te).

energy and 10^{-4} e for charge was adopted. Phonon dispersion curves were calculated by interfacing WIEN2k with the Phonopy package[26]. Supercells with small atomic displacements were generated, and atomic forces were computed using WIEN2k for each configuration. These forces were then used by Phonopy to construct the dynamical matrix and extract phonon frequencies across the Brillouin zone. Optical properties were calculated through the computation of the complex dielectric tensor components $\varepsilon(\omega) = \varepsilon_1(\omega) + i\varepsilon_2(\omega)$. Subsequently, other optical properties such as the refractive index $n(\omega)$, absorption coefficient $\alpha(\omega)$, and optical conductivity $\sigma(\omega)$ were derived from the dielectric tensor components. Finally, thermoelectric properties were calculated using the semi-classical Boltzmann theory and the relaxation time approximation implemented in the BoltzTraP interface[27] integrated with the Wien2k package. The Seebeck coefficient S(T), electrical conductivity σ(T), and electronic thermal conductivity κe(T) were evaluated as functions of temperature, and the figure of merit $ZT = S^2\sigma T/\kappa$ was calculated.

Results and discussion

Structural properties

Figure 1; Schematic crystal structures of (a) $LiInS_2$ and (b) $LiInTe_2$. (a) $LiInS_2$ crystallizes in an orthorhombic system with space group $Pna2_1$ (No. 33). In this structure, the lithium (Li) atoms typically occupy the **4a** Wyckoff position, indium (In) atoms occupy the **4a** position, and sulfur (S) atoms are located at **8b (**positions. The structure consists of slightly distorted tetrahedra formed by InS_4 and LiS_4 units interconnected in a three-dimensional framework. (b) $LiInTe_2$ crystallizes in a tetragonal system with space group I-42d (No. 122). In this phase, lithium (Li) atoms occupy the **4a** Wyckoff positions, indium (In) atoms are located at **4b**, and tellurium (Te) atoms are situated at **8d** positions. The crystal structure is composed of $InTe_4$ and $LiTe_4$ tetrahedra arranged symmetrically in a tetragonal lattice.

The lattice constants of $LiInX_2$ (X = S, Te) compounds were optimized by calculating the total energy of the system as a function of the unit cell volume, as shown in Fig. 2.

By fitting the energy-volume relationship using the Murnaghan equation of state, the equilibrium values for lattice constants, bulk modulus B, and pressure derivative of bulk modulus B' were obtained. For $LiInS_2$, the calculated lattice constants for this compound are a = 6.93 Å, b = 8.088 Å, and c = 6.519 Å, which are close to the published experimental values[1] (a = 6.874 Å, b = 8.064 Å, and c = 6.46 Å) with a difference not exceeding 1%. On the other hand, in $LiInTe_2$ compounds, the calculated lattice constants are a = 6.498 Å and b = 12.25 Å, which are also close to the experimental values[2] (a = 6.39 Å and b = 12.46 Å) with a difference of about 1.7% for a and 1.7% for b. The bulk modulus B reflects the material's resistance to deformation under external pressure. The calculated B value is 61.92 GPa for $LiInS_2$ and 34.075 GPa for $LiInTe_2$. These values indicate that $LiInS_2$ is more rigid than $LiInTe_2$, which is expected given the larger size of Te atoms compared to S atoms, resulting in weaker and more flexible bonds in the case of $LiInTe_2$.To verify the dynamic stability of the compounds, phonon dispersion was calculated and is shown in Fig. 3.

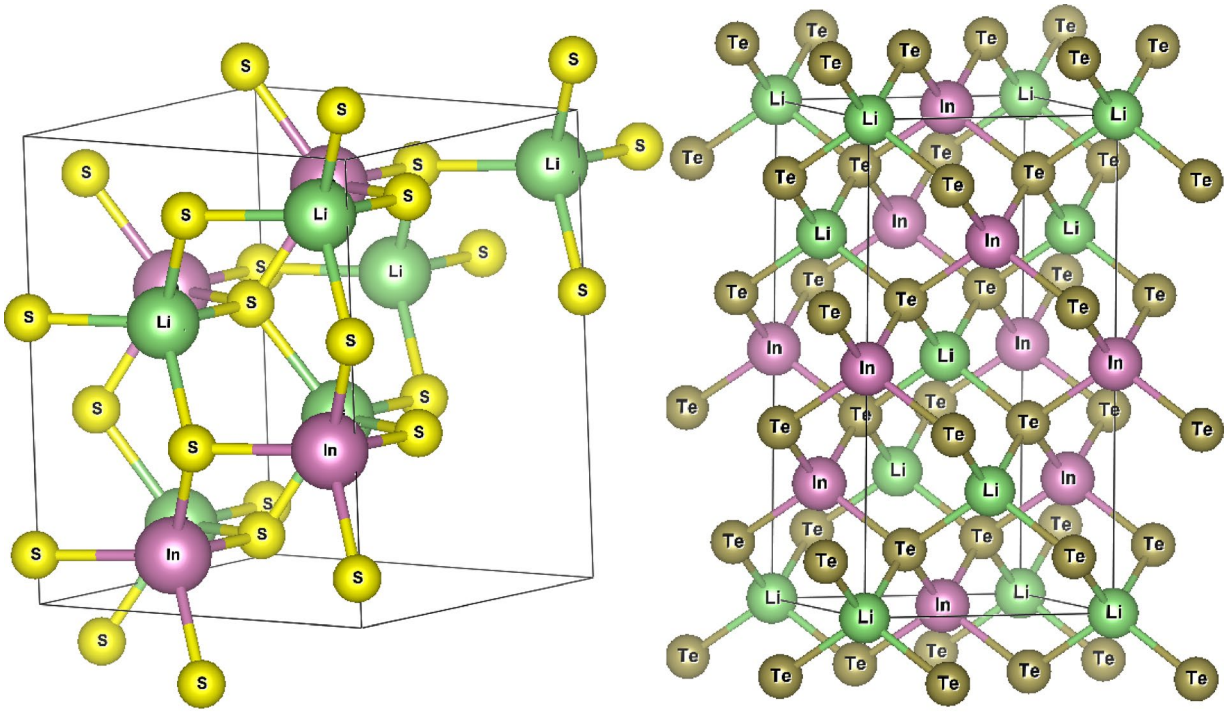

Fig. 1. The calculated energy vs. volume curves for optimizing of $LiInX_2$ (X = S, Te) using GGA approximation.

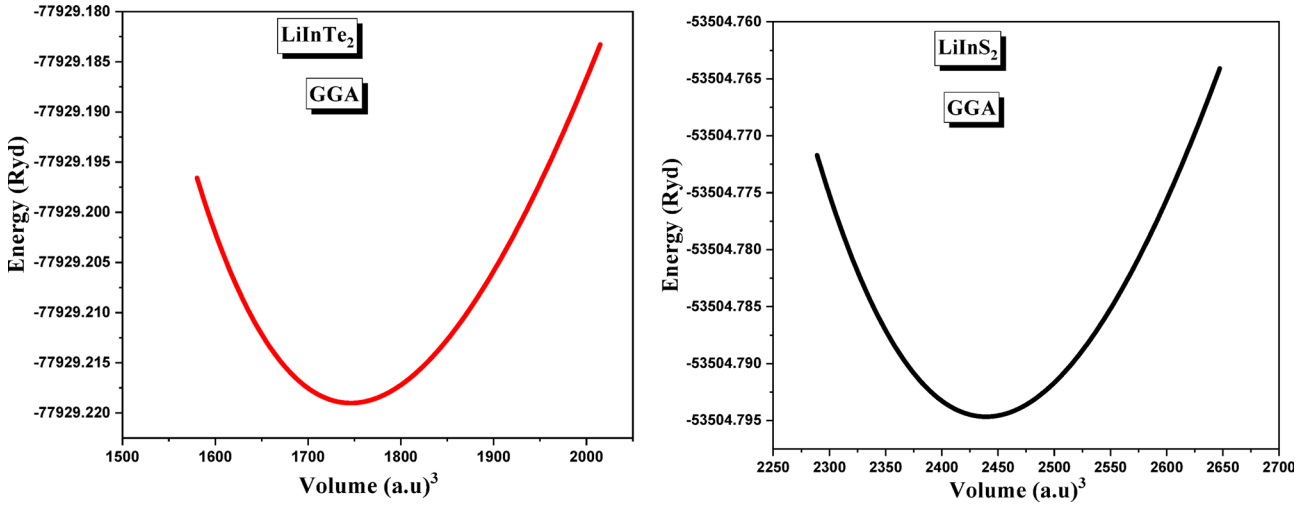

Fig. 2. The calculated energy vs. volume curves for optimizing of $LiInX_2$ (X = S, Te) using GGA approximation.

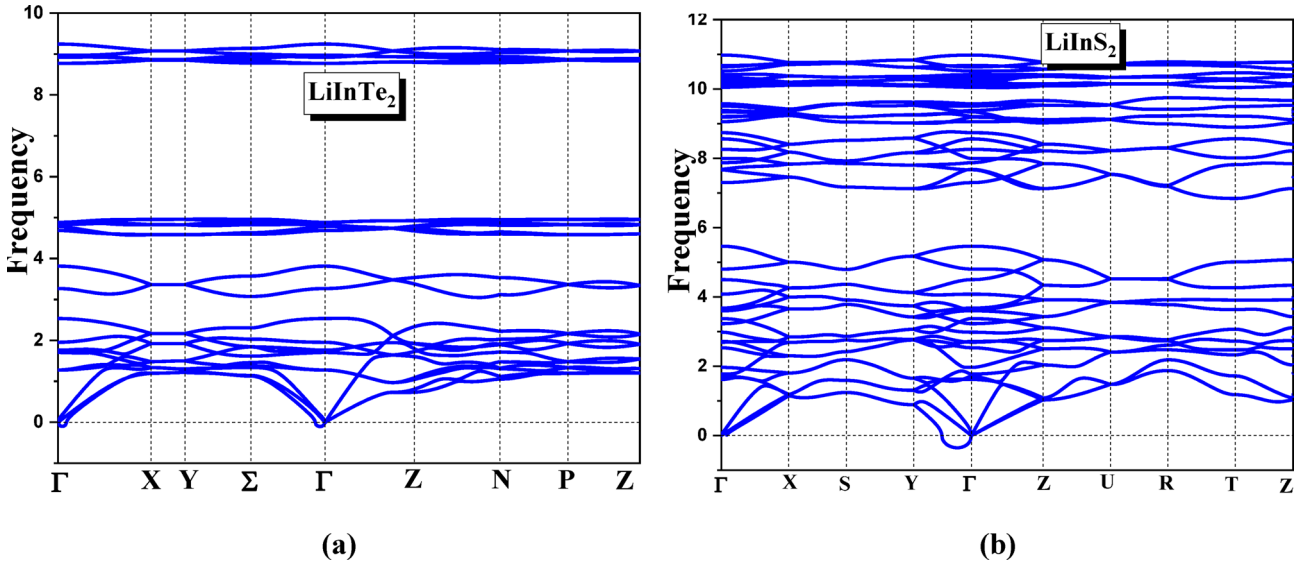

Fig. 3. Phonon dispersions for (**a**)$LiInS_2$, (**b**)$LiInTe_2$computed by Phononpy Using GGA approximation.

The phonon dispersion curves for $LiInS_2$ show no imaginary frequencies, indicating clear dynamic stability. For $LiInTe_2$, although the acoustic branches near the Γ point are very soft, they remain positive, suggesting marginal but sufficient dynamic stability under ambient pressure. Furthermore, the acoustic branches exhibit a linear dispersion near the Γ point, which is indicative of stable lattice vibrations. The relatively low maximum phonon frequencies observed in $LiInTe_2$, compared to $LiInS_2$, can be attributed to the heavier atomic mass of Te. This phonon behavior is expected to influence the lattice thermal conductivity and thermoelectric performance, as lower phonon frequencies typically correspond to reduced phonon group velocities and hence lower thermal conductivity a desirable feature for thermoelectric materials.

Mechanical properties

Elastic constants and stability

The calculated elastic constant matrices for both compounds are presented in Table 2. For $LiInS_2$, which crystallizes in an orthorhombic structure, nine independent elastic constants are required by symmetry. In contrast, $LiInTe_2$, with its tetragonal structure, only necessitates six independent constants due to its higher symmetry.

The elastic constants reveal notable trends. Most significantly, the diagonal terms C_{11}, C_{22}, C_{33} of $LiInS_2$ are markedly higher than those of $LiInTe_2$, indicating a superior resistance to longitudinal deformation in $LiInS_2$. The most dramatic decrease occurs in C_{33}, which drops from 126.76 GPa in $LiInS_2$ to 41.15 GPa in $LiInTe_2$ a reduction of approximately 67%. This indicates a pronounced softness of $LiInTe_2$ along the c-axis. Interestingly,

	LiInS2	LiInTe2
C_{11}	115.949	53.080
C_{12}	34.649	32.355
C_{13}	19.369	33.842
C22	114.341	/
C23	22.047	/
C33	126.760	41.146
C_{44}	27.774	37.738
C55	24.869	/
C_{66}	41.522	36.763
B_H	56.573	38.223
G_H	36.157	19.634
E_H	89.421	50.290
ν_H	0.237	0.281
B_H/G_H	1.564	1.946
Average elastic wave velocity (m/s)	3626.522	2244.739
Debye Temperature Θ_D(K)	380.515	209.751

Table 2. Single crystal elastic constants, cij, bulk modulus B_H(in GPa), shear modulus G (in GPa), Young's modulus EH (in GPa), Poisson's coefficient ν_H(GPa), Pugh's modulus ratio B_H/G_H of $LiInX_2$ (X = S, Te).

the shear constants C_{44} and C_{66} are higher in $LiInTe_2$, suggesting enhanced resistance to shear in specific planes compared to $LiInS_2$. All calculated constants meet the Born-Huang mechanical stability criteria, confirming the mechanical stability of both compounds under ambient conditions.

For completeness, the mechanical stability conditions used are as follows[28]:

- For orthorhombic systems ($LiInS_2$).

$C_{11}>0$, $C_{22}>0$, $C_{33}>0$, $C_{44}>0$, $C_{55}>0$, $C_{66}>0$.
$C_{11}+C_{22}-2C_{12}>0$.
$C_{11}+C_{33}-2C_{13}>0$.
$C_{22}+C_{33}-2C_{23}>0$.
$C_{11}+C_{22}+C_{33}+2(C_{12}+C_{13}+C_{23})>0$.

- For tetragonal systems ($LiInTe_2$).

$C11>|C12|$, $C33>0$, $C44>0$, $C66>0$.
$C11+C33-2C13>0$, $2(C11+C12)+C33+4C13>0$.

Mechanical properties and Brittleness–Ductility analysis

The Voigt-Reuss-Hill (VRH) averaged mechanical properties reveal significant differences between the compounds. $LiInS_2$ exhibits a bulk modulus of 56.57 GPa, 48% higher than that of $LiInTe_2$ (38.22 GPa), reflecting stronger resistance to volume change. The shear modulus difference is even more pronounced: 36.16 GPa for $LiInS_2$ compared to only 19.63 GPa for $LiInTe_2$ an 84% reduction. Young's modulus follows a similar trend: 89.42 GPa for $LiInS_2$ and 50.29 GPa for $LiInTe_2$. These values indicate that $LiInS_2$ is significantly stiffer and better suited for applications requiring dimensional stability under load. The Pugh's ratio (B/G) differentiates the ductility of the materials. $LiInS_2$, with a ratio of 1.564, is classified as brittle, while $LiInTe_2$, with a value of 1.946, lies in the ductile regime. This transition in mechanical behavior is attributed to the nature of chemical bonding. The sulfur-based compound exhibits stronger covalent interactions that impede dislocation movement, promoting brittle failure. In contrast, the tellurium compound's more metallic bonding allows easier plastic deformation.

Structure property relationships: anisotropy, acoustic, thermal, and hardness trends

To gain a holistic understanding of the mechanical behavior, we analyze additional structure-sensitive properties such as elastic anisotropy, sound velocities, thermal behavior, and predicted hardness.

A- **Elastic Anisotropy**: Using the Ranganathan–Shivakumar and Kube indices, $LiInS_2$ shows moderate anisotropy (A_R = 0.405, A_K = 0.174), while $LiInTe_2$ exhibits high anisotropy (A_R = 4.384, A_K = 1.403). These findings are visually supported by the three-dimensional plots in Figs. 4 and 5, which display the directional dependence of mechanical properties.

Figure 4 illustrates the 3D distributions of Poisson's ratio, bulk modulus, shear modulus, and Young's modulus for **$LiInTe_2$**, highlighting its highly anisotropic elastic response.

Figure 5 presents the corresponding elastic surfaces for $LiInS_2$, revealing a more isotropic and mechanically uniform behavior.

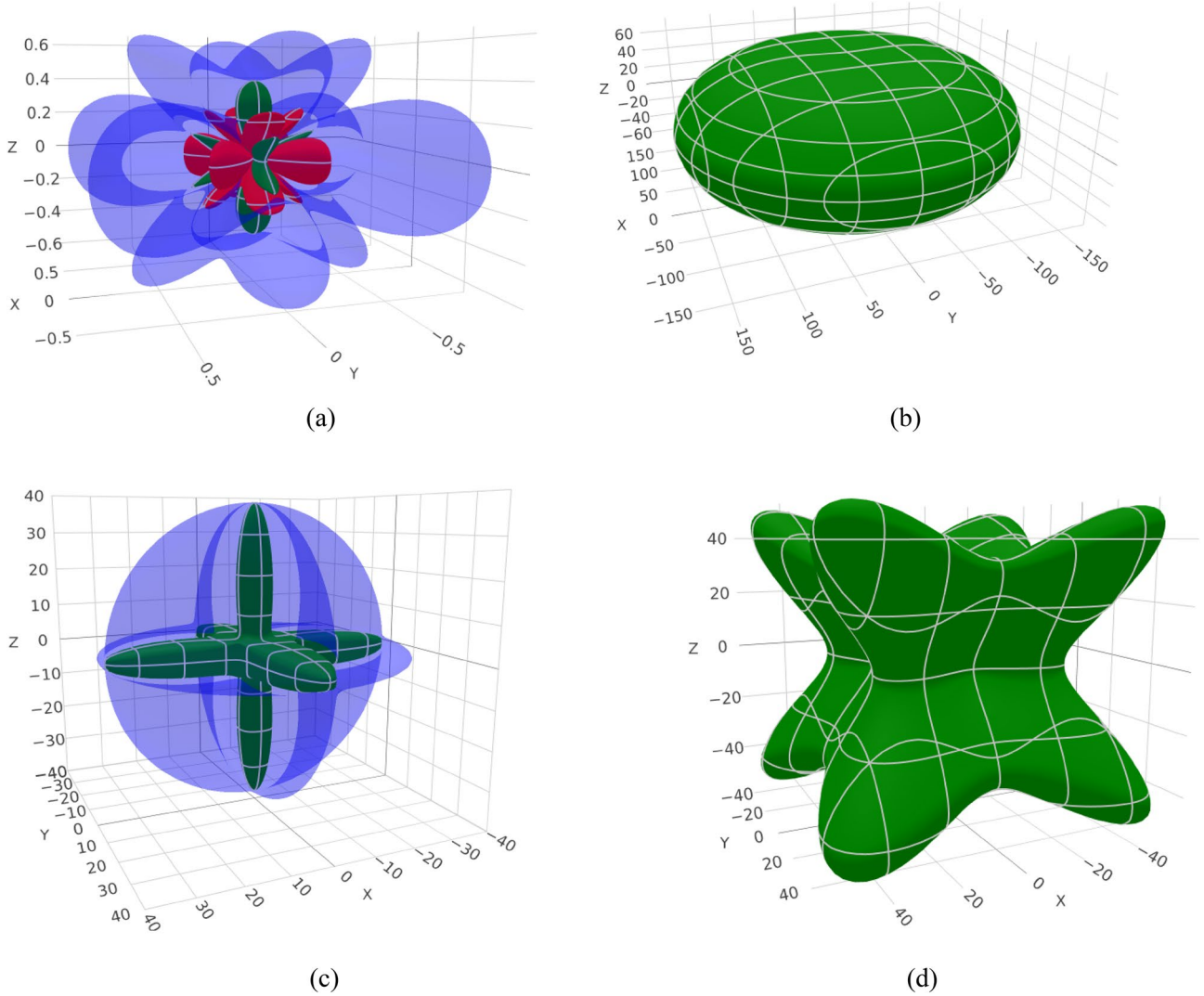

Fig. 4. The 3D distributions of Poisson's ratio, bulk modulus, shear modulus, and Young's modulus for $LiInTe_2$.

B- acoustic and thermal behavior The average elastic wave velocity in $LiInS_2$ (3626.5 m/s) is significantly higher than in $LiInTe_2$ (2244.7 m/s), aligning with its greater stiffness. Correspondingly, the Debye temperature of $LiInS_2$ is 380.5 K, almost double that of $LiInTe_2$ (209.8 K), implying stronger atomic bonding and better thermal resistance.

C- hardness predictions The Vickers hardness values, estimated using the Chen and Tian models, reveal that $LiInS_2$ is approximately three times harder than $LiInTe_2$. These results correlate well with the differences in elastic moduli and support the interpretation of bonding strength and deformation resistance.

Electronic properties

The electronic band structure for $LiInX_2$ (X = S, Te) compounds were calculated using mBJ-GGA approximations and are shown in **Fig.** 6.

Analysis of the band structure reveals that both compounds possess direct band gaps at the Γ point in the Brillouin zone. Using the GGA approximation, the band gap values were found to be 2.439 eV for $LiInS_2$ and 1.661 eV for $LiInTe_2$, as shown in Table 3. However, it is well known that the GGA approximation tends to underestimate the band gap value. To obtain more accurate band gap values, we employed the TB-mBJ (Tran-Blaha modified Becke-Johnson) potential. Unlike standard GGA functionals which often underestimate the band gap due to self-interaction errors and the lack of derivative discontinuity, TB-mBJ corrects these limitations and yields results in closer agreement with experimental observations. This makes TB-mBJ particularly suitable for studying the electronic and optical properties of semiconducting materials, the band gap values increased to 3.61 eV for $LiInS_2$ and 2.33 eV for $LiInTe_2$, which are very close to the published experimental values (3.59 eV[1] and 2.34 eV[3], respectively). Analysis of the total and partial density of states (PDOS) shown in Figs. 7 and 8 reveals that the upper valence band of $LiInS_2$ consists mainly of S *3p* states with a small contribution from In *5s* states, while the lower conduction band consists primarily of In 5 s states. In the case of $LiInTe_2$, Te 5p states

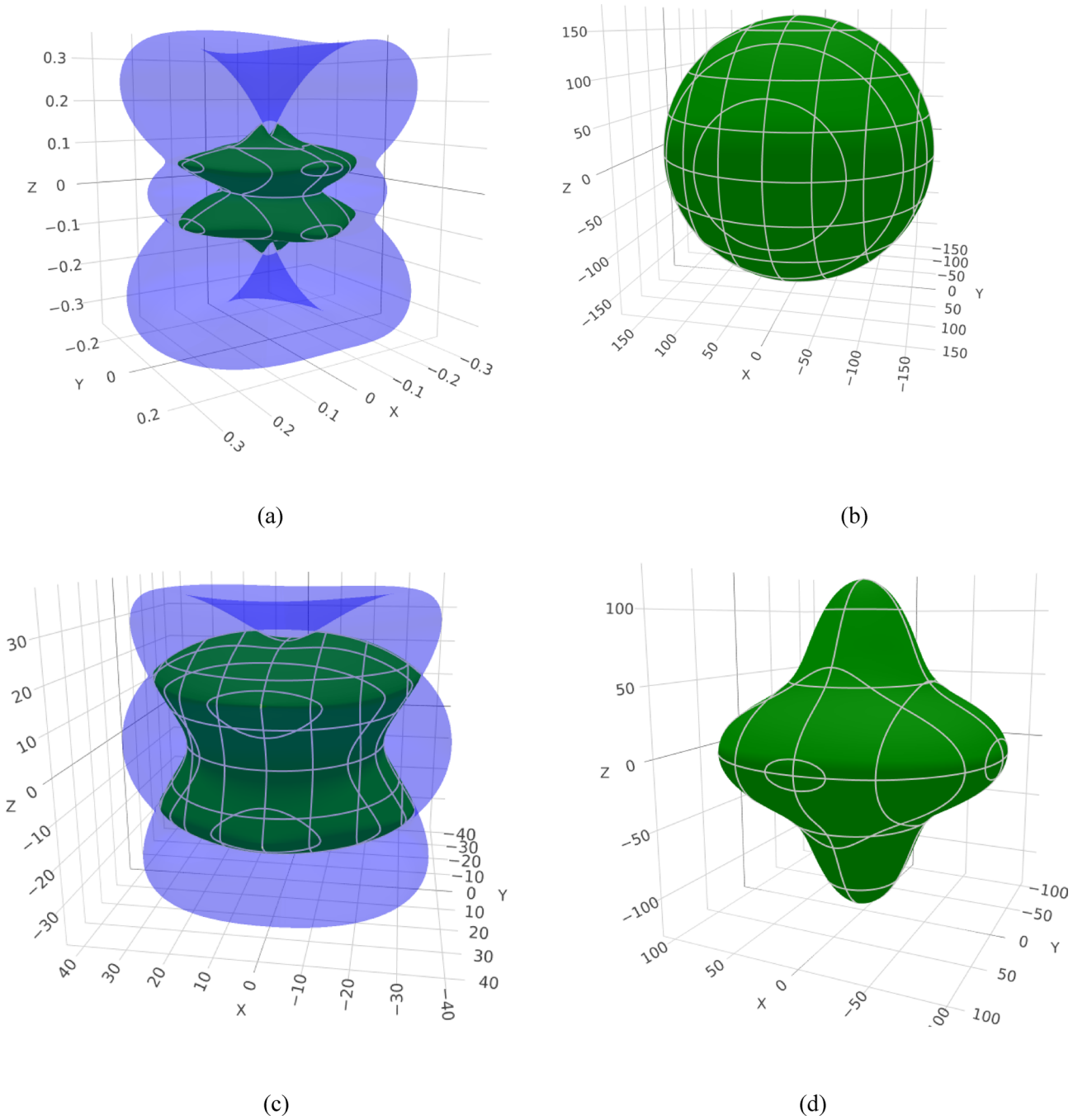

Fig. 5. The 3D distributions of Poisson's ratio, bulk modulus, shear modulus, and Young's modulus for **$LiInS_2$**.

dominate the upper valence band, while the lower conduction band mainly consists of In *5s* and Te *5p* states. The difference in band gap between the two compounds can be attributed to the difference in chemical bonding and atomic size. Te atoms are larger than S atoms, leading to weaker orbital overlap and consequently a smaller band gap in the case of $LiInTe_2$. This difference in band gap makes the two compounds suitable for different applications: $LiInS_2$ for optical device applications in the visible range, and $LiInTe_2$ for applications in the near-infrared range.

Optical properties

The optical properties of $LiInX_2$ (X = S, Te) compounds were calculated in the photon energy range from 0 to 20 eV using the mBJ-GGA approximation. The energy range of 0–20 eV was selected to cover all significant interband transitions, including those in the visible and ultraviolet regions. This range ensures a comprehensive analysis of the material's optical response. The optical properties such as the dielectric function, absorption coefficient (α), reflectivity (R), refractive index (n), and energy loss function (L) were calculated using standard

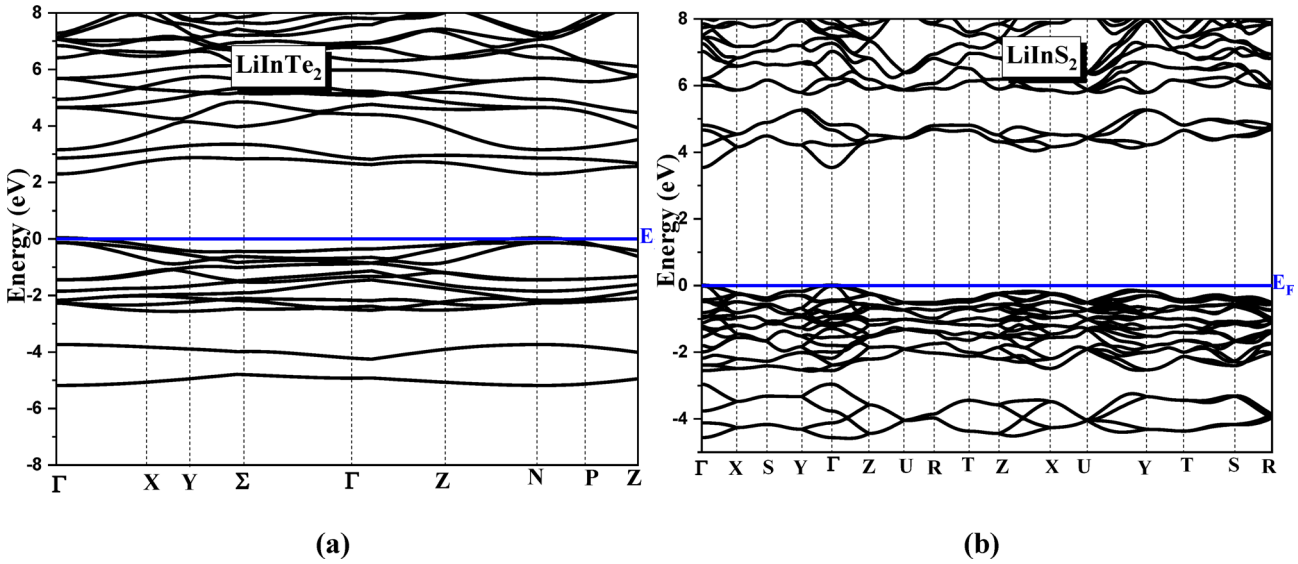

Fig. 6. The electronic band structure (**a**)$LiInS_2$, (**b**)$LiInTe_2$Using mBJ-GGA.

	GGA	mBJ
$LiInS_2$	2.439	3.61 3.59exp[1]
LiInTe2	1.661	2.33 2.34[3]

Table 3. The band gap $LiInX_2$ (X = S, Te)usingGGA, and mBJ.

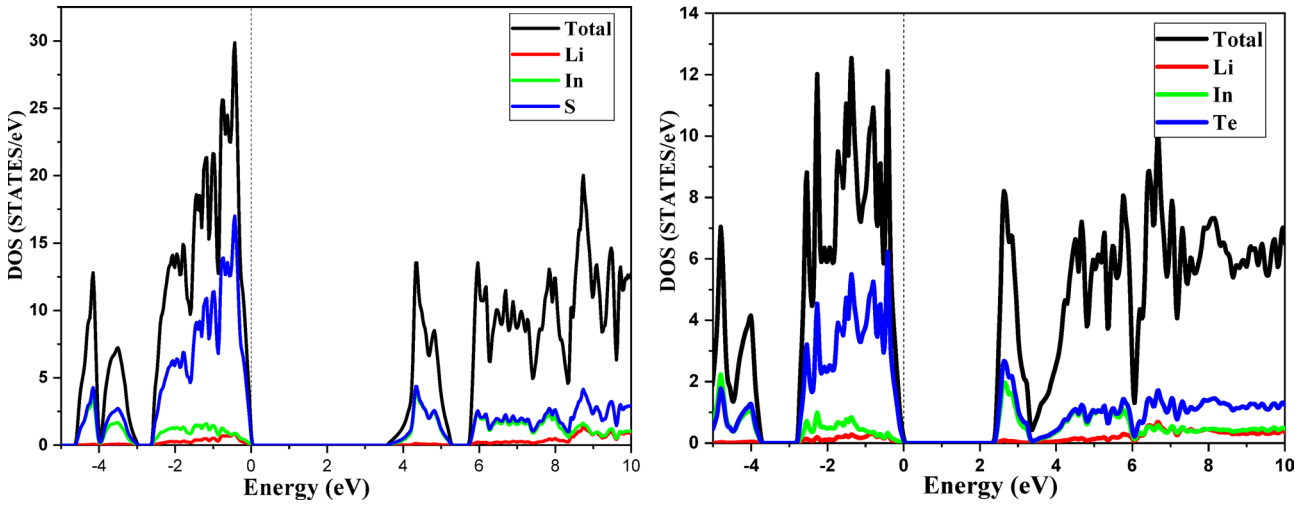

Fig. 7. The density of states of (**a**)$LiInS_2$, (**b**)$LiInTe_2$Using mBJ-GGA.

relations as detailed in[29–32]. These properties provide insight into how the material interacts with electromagnetic radiation across various energy ranges. Figures 9 and 10 present the complex dielectric function, refractive index, extinction coefficient, energy loss function, absorption coefficient, optical conductivity, and reflectivity for both compounds. The real part of the dielectric function $\varepsilon_1(\omega)$ for $LiInS_2$ is characterized by a static dielectric constant ($\omega \rightarrow 0$) of approximately 5.8, while this value is about 8.2 for $LiInTe_2$. This difference is consistent with the general rule that materials with smaller band gaps tend to have larger dielectric constants. The dielectric function is intimately related to the electronic band structure. The imaginary part, $\varepsilon_2(\omega)$, represents interband electronic transitions, and its peaks correspond to energies where such transitions are allowed. The real part, $\varepsilon_1(\omega)$, obtained via the Kramers-Kronig transformation, provides insight into the material's polarizability. Thus,

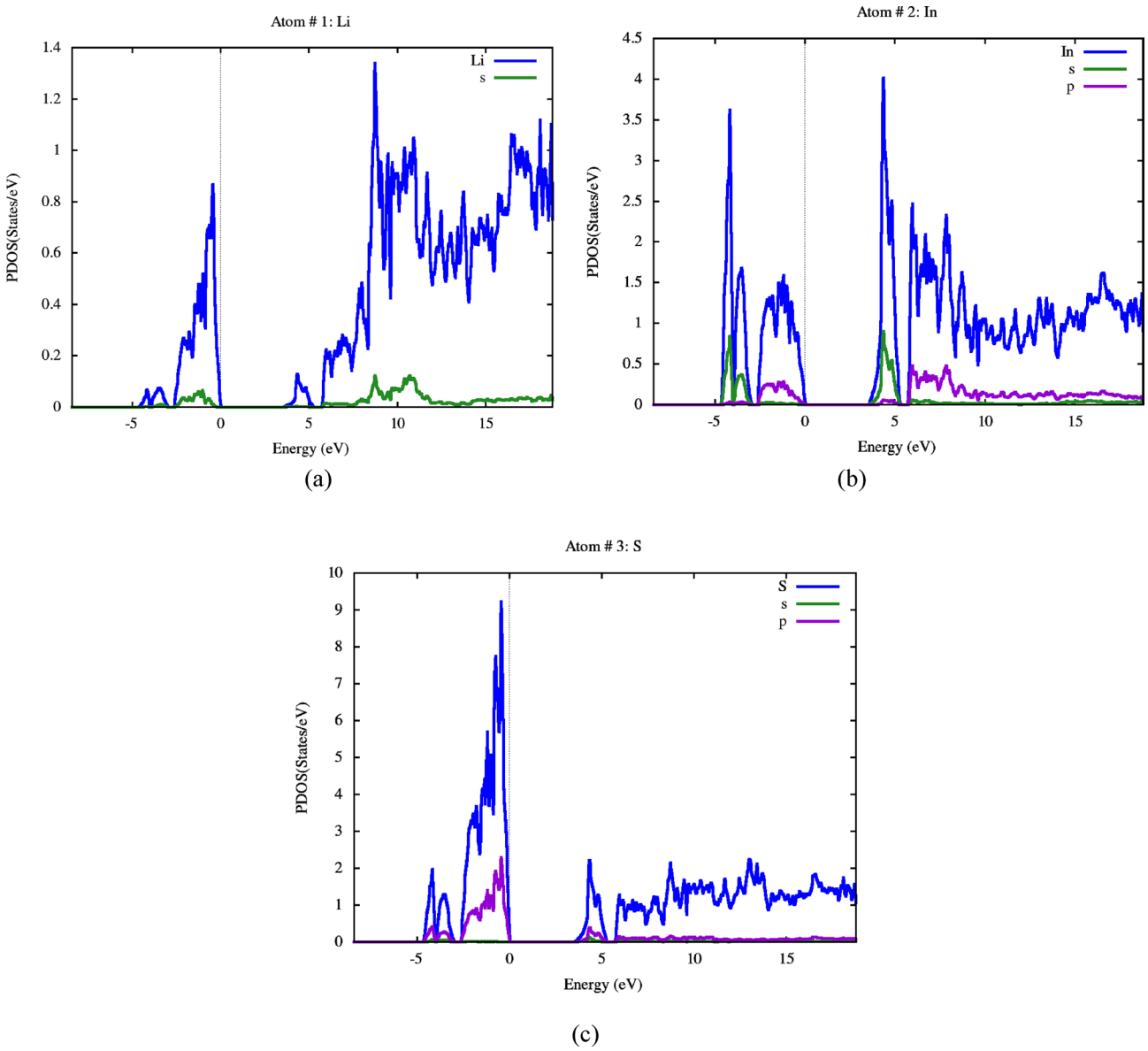

Fig. 8. Partial density of states of $LiInS_2$.

the optical response reflects the underlying electronic properties such as the band gap and density of states. In the case of $LiInS_2$, the first sharp peak appears at about 4 eV, corresponding to direct transitions from S *3p* states to In *5s* states. In the case of $LiInTe_2$, the first peak appears at about 2.5 eV, reflecting transitions from Te *5p* states to In *5s* states. The negative values observed in the real part of the dielectric function $\varepsilon_1(\omega)$ at high photon energies can be attributed to a plasmonic-type response, where the material exhibits metallic behavior and strong reflection. In this energy range, the electromagnetic wave cannot propagate through the material, leading to a reflective optical regime. Such features are significant for designing UV reflectors and other photonic devices. The static refractive index n(0) is approximately 2.4 for $LiInS_2$ and 2.9 for $LiInTe_2$. These values are important for optical device applications such as anti-reflection coatings and optical filters. The absorption coefficient $\alpha(\omega)$ begins to rise sharply at a photon energy equal to the direct band gap of each compound and reaches high values ($>10^5$ cm^{-1}) in the ultraviolet range, indicating strong light absorption in this range. Each peak in the absorption coefficient and the dielectric function can be associated with specific interband electronic transitions. These transitions are influenced by the density of states and the band structure, especially near the Fermi level. Moreover, the anisotropy observed in the optical response along the xx and yy directions reflects the non-cubic symmetry of the crystal structure. The increase in absorption at lower photon energies corresponds to direct electronic transitions from the valence to conduction bands near the band edges. As the photon energy increases beyond these regions, the density of accessible electronic states decreases, leading to a gradual decline in the absorption coefficient. The energy loss function shows a main peak (plasmon peak) at about 16 eV for $LiInS_2$ and 14 eV for $LiInTe_2$, reflecting the frequency at which collective oscillation of electrons occurs. The optical conductivity $\sigma(\omega)$ is a measure of the material's response to the electric field of incident light and shows

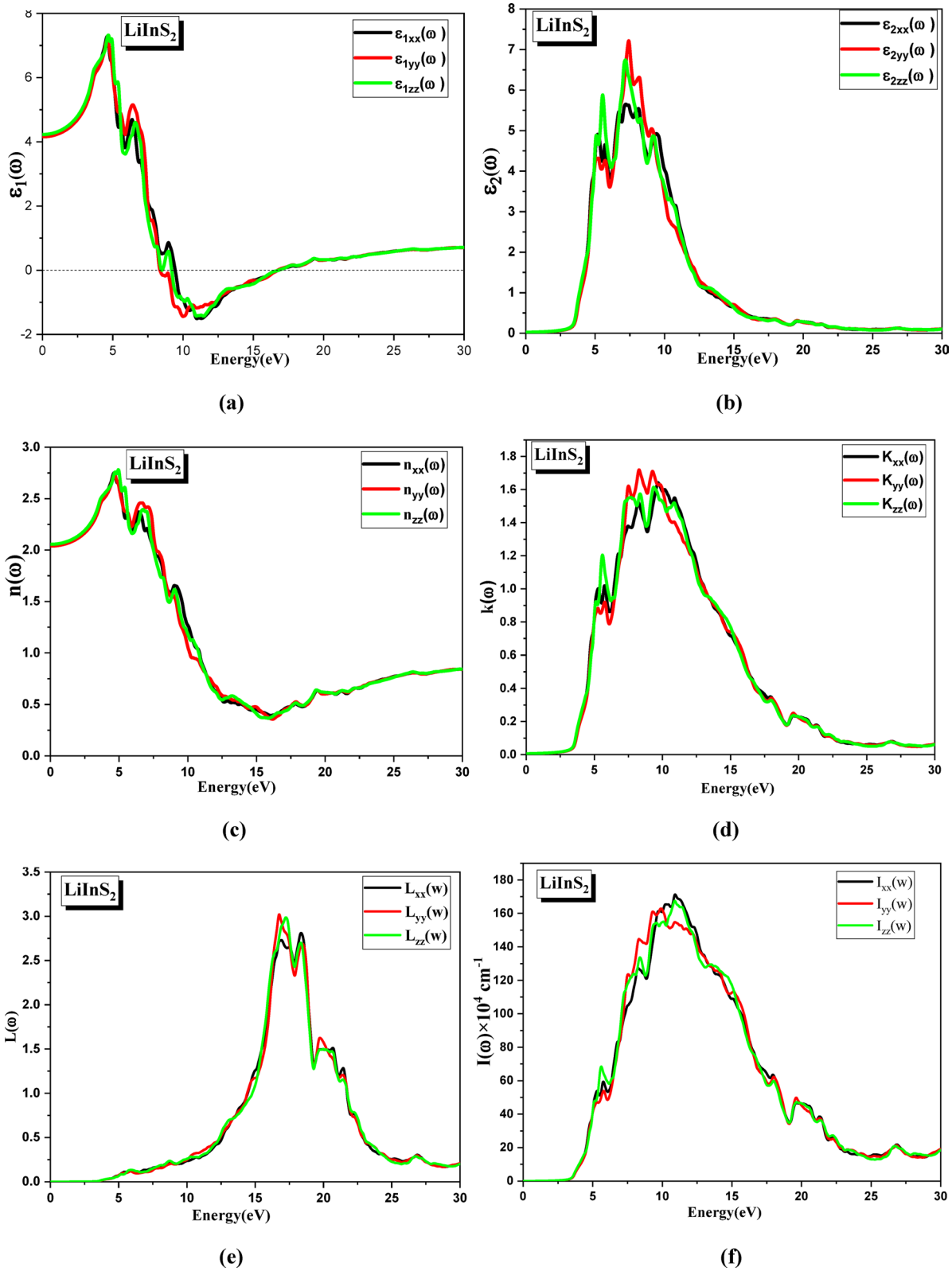

Fig. 9. The real (**a**) and imaginary (**b**) components of the dielectric function, the refractive index (**c**), the extinction coefficient (**d**), the energy loss (**e**), and the absorption coefficient (**f**). The real optical conductivity (**g**) and reflectivity (**h**) as functions of photon energy for $LiInS_2$usingmBJ-GGA.

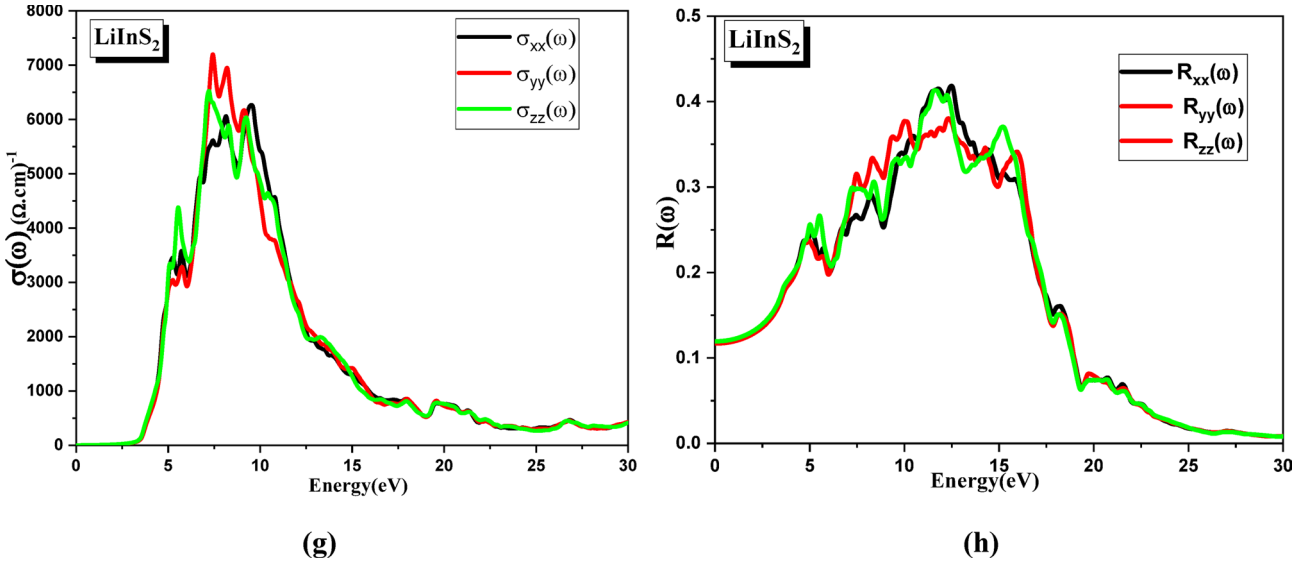

Fig. 9. (continued)

peaks corresponding to the peaks of $\varepsilon_2(\omega)$. Finally, the static reflectivity R(ω) is about 0.17 for $LiInS_2$ and 0.24 for $LiInTe_2$. The reflectivity increases with increasing photon energy and reaches high values in the far ultraviolet range. A comparison of the optical spectra along the xx, yy, and zz directions reveals clear anisotropic behavior, consistent with the orthorhombic symmetry of the $LiInX_2$ crystal structure. While the xx and yy components often exhibit similar trends, the zz component displays noticeable variations in peak positions and intensities across different optical parameters—including the dielectric function, absorption coefficient, refractive index, and reflectivity. This directional dependence arises from the structural asymmetry and highlights the importance of polarization and crystallographic orientation in potential optoelectronic applications.

Thermoelectric properties

The thermoelectric properties of $LiInX_2$ (X = S, Te) compounds were calculated in the temperature range from 300 to 900 K and are shown in Figs. 11 and 12. These properties include the Seebeck coefficient S(T), figure of merit ZT, electronic thermal conductivity κe(T), total thermal conductivity κ(T), magnetic susceptibility, and power factor $PF = S^2\sigma$. It is worth noting that the thermoelectric properties were calculated in the temperature range from 300 K to 900 K, well below the melting points of $LiInS_2$ (~ 1120 K) and $LiInTe_2$. The structural stability observed in this range is thus consistent with their experimentally reported high thermal endurance, reinforcing their suitability for high-temperature thermoelectric applications. The Seebeck coefficient S(T) shows positive values for both compounds, indicating that hole-dominated charge transport mechanisms (positive charge carriers) are dominant. The value of S(T) decreases with increasing temperature, which is typical behavior for semiconductors. At a temperature of 300 K, the value of S(T) is about 250 μV/K for $LiInS_2$ and 220 μV/K for $LiInTe_2$, which are good values compared to conventional thermoelectric materials. The electronic thermal conductivity κe(T) increases with increasing temperature for both compounds, while the total thermal conductivity κ(T) shows more complex behavior due to the phonon contribution. The value of κ(T) at a temperature of 300 K is about 2 W/m·K for $LiInS_2$ and 1.5 W/m·K for $LiInTe_2$, which are relatively low values that enhance the efficiency of thermoelectric conversion. The magnetic susceptibility (χ″) of $LiInS_2$ and $LiInTe_2$ was analyzed across temperatures (300–900 K). $LiInS_2$ shows strong peaks near − 1.5 eV and 5 eV, with sharp features at low temperatures that diminish with heating, indicating thermally damped magnetic excitations. $LiInTe_2$ exhibits flatter, less intense spectra, with major features around − 1 eV and 3 eV, and weaker thermal sensitivity. The stronger response of $LiInS_2$ suggests enhanced electronic correlations or localized moments. In contrast, $LiInTe_2$'s behavior reflects a more stable, less magnetically active system. Both materials follow expected thermal trends of reduced susceptibility with temperature. Overall, $LiInS_2$ is more promising for temperature-sensitive magneto-electronic applications. The figure of merit ZT is a measure of thermoelectric conversion efficiency, with higher values indicating better efficiency. ZT increases with increasing temperature for both compounds, reaching about 0.6 for $LiInS_2$ and 0.8 for $LiInTe_2$ at a temperature of 800 K. These values are promising and indicate the potential use of these compounds in thermoelectric energy conversion applications, especially at high temperatures. The power factor $PF = S^2\sigma$, another measure of thermoelectric performance, shows increasing values with increasing temperature, further enhancing the attractiveness of these compounds for thermoelectric power generation applications.

Conclusion

In this study, a comprehensive analysis of the structural, electronic, optical, and thermoelectric properties of $LiInX_2$ (X = S, Te) compounds were conducted using first-principles calculations based on density functional theory. We reached the following main conclusions:

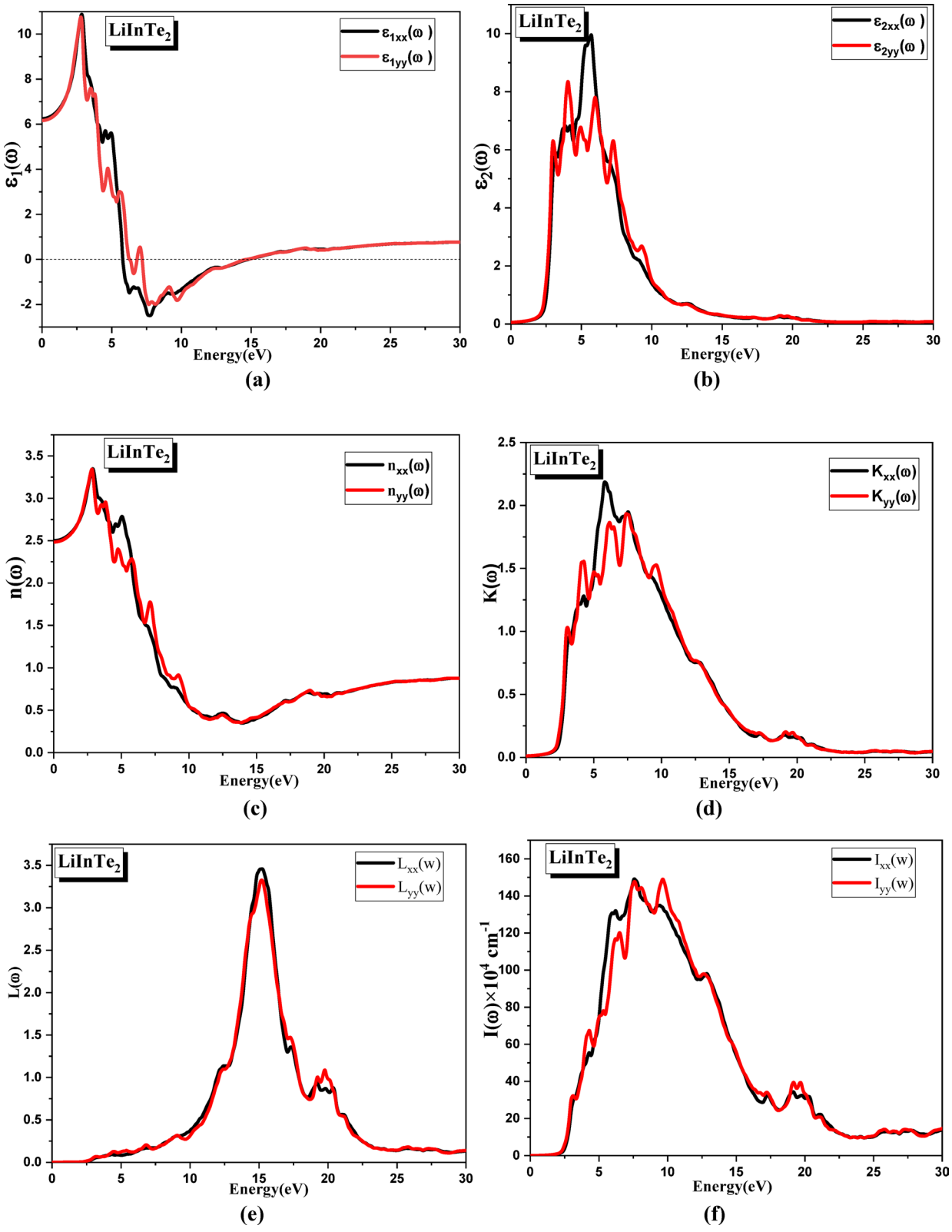

Fig. 10. The real (**a**) and imaginary (**b**) components of the dielectric function, the refractive index (**c**), the extinction coefficient (**d**), the energy loss (**e**), and the absorption coefficient (**f**). The real optical conductivity (**g**) and reflectivity (**h**) as functions of photon energy for $LiInTe_2$usingmBJ-GGA.

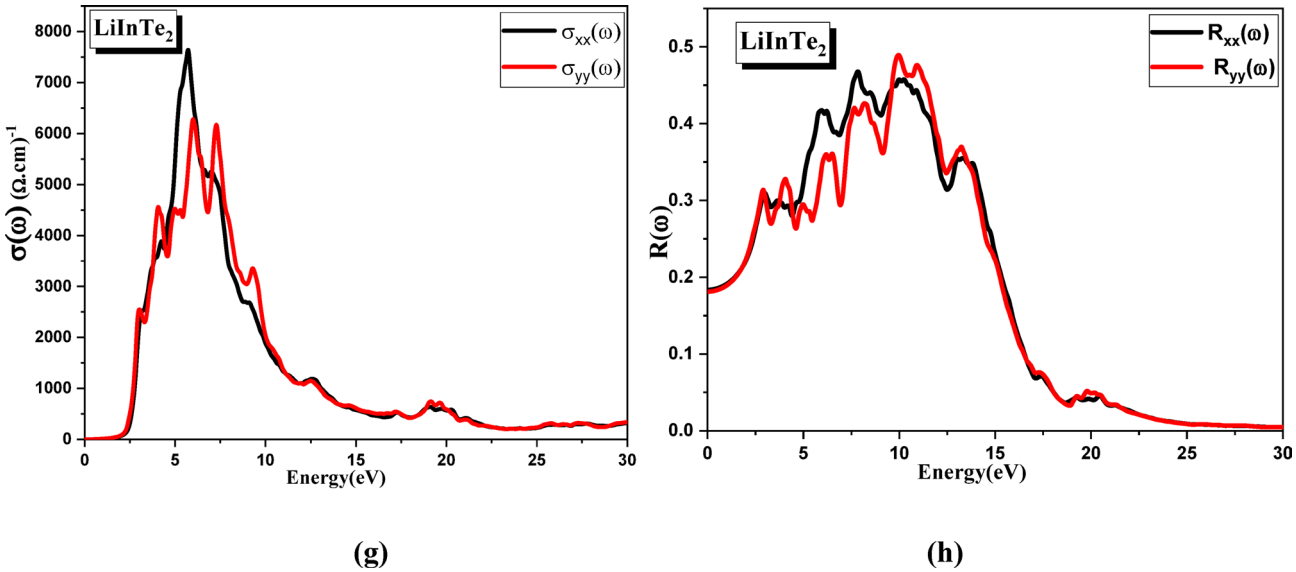

(g) (h)

Fig. 10. (continued)

- $LiInS_2$ crystallizes in an orthorhombic system with space group Pna21, while $LiInTe_2$ crystallizes in a tetragonal system with space group I-42d. The calculated lattice constants show good agreement with published experimental values, with a difference not exceeding 1.7%.
- Both compounds possess direct band gaps at the Γ point in the Brillouin zone. Using the mBJ-GGA approximation, the band gap values were found to be 3.61 eV for $LiInS_2$ and 2.33 eV for $LiInTe_2$, which are very close to the experimental values. This confirms that the mBJ-GGA approximation is more accurate than the traditional GGA approximation in describing the electronic properties of these compounds.
- Analysis of the partial density of states reveals that the upper valence band in $LiInS_2$ consists mainly of S 3p states, while the lower conduction band consists of In 5s states. In the case of $LiInTe_2$, Te 5p states dominate the upper valence band.
- The calculated optical properties show that both compounds have relatively high static refractive indices (2.4 for $LiInS_2$ and 2.9 for $LiInTe_2$) and high absorption coefficients in the ultraviolet range, making them promising candidates for optical device applications.
- The thermoelectric properties indicate that both compounds have positive Seebeck coefficients and relatively low thermal conductivity, resulting in promising values for the figure of merit ZT, especially at high temperatures (0.6 for $LiInS_2$ and 0.8 for $LiInTe_2$ at 800 K).
- The mechanical stability and elastic resilience of $LiInS_2$ further support its potential use in high-durability optoelectronic devices.

Based on these results, it can be concluded that $LiInX_2$ (X = S, Te) compounds possess promising physical properties that make them candidates for multiple applications. $LiInS_2$, with its wide band gap, can be used in optical device applications in the visible range, such as tunable lasers and second harmonic converters. Meanwhile, $LiInTe_2$, with its smaller band gap, can be used in near-infrared applications. The good thermoelectric properties of both compounds can also be exploited in energy conversion applications, especially at high temperatures.

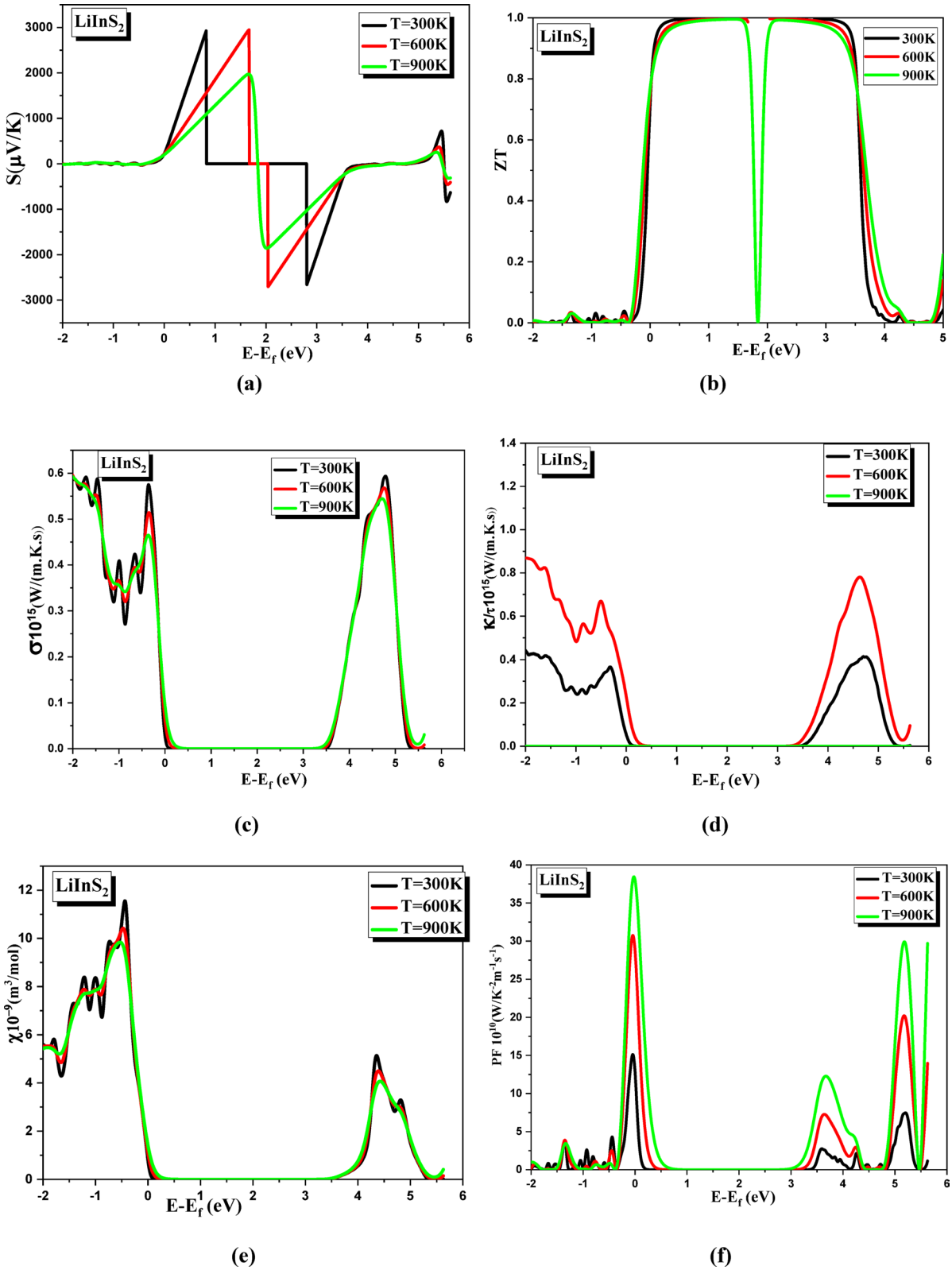

Fig. 11. (**a**)the Seebeck coefficient, (**b**) the figure of merit ZT, (**c**) electronic thermal conductivity, (**d**) the thermal conductivity, (**e**)Magnetic susceptibility, (**f**)Power Factorwithin the mBJ-GGA approximationfor $LiInS_2$.

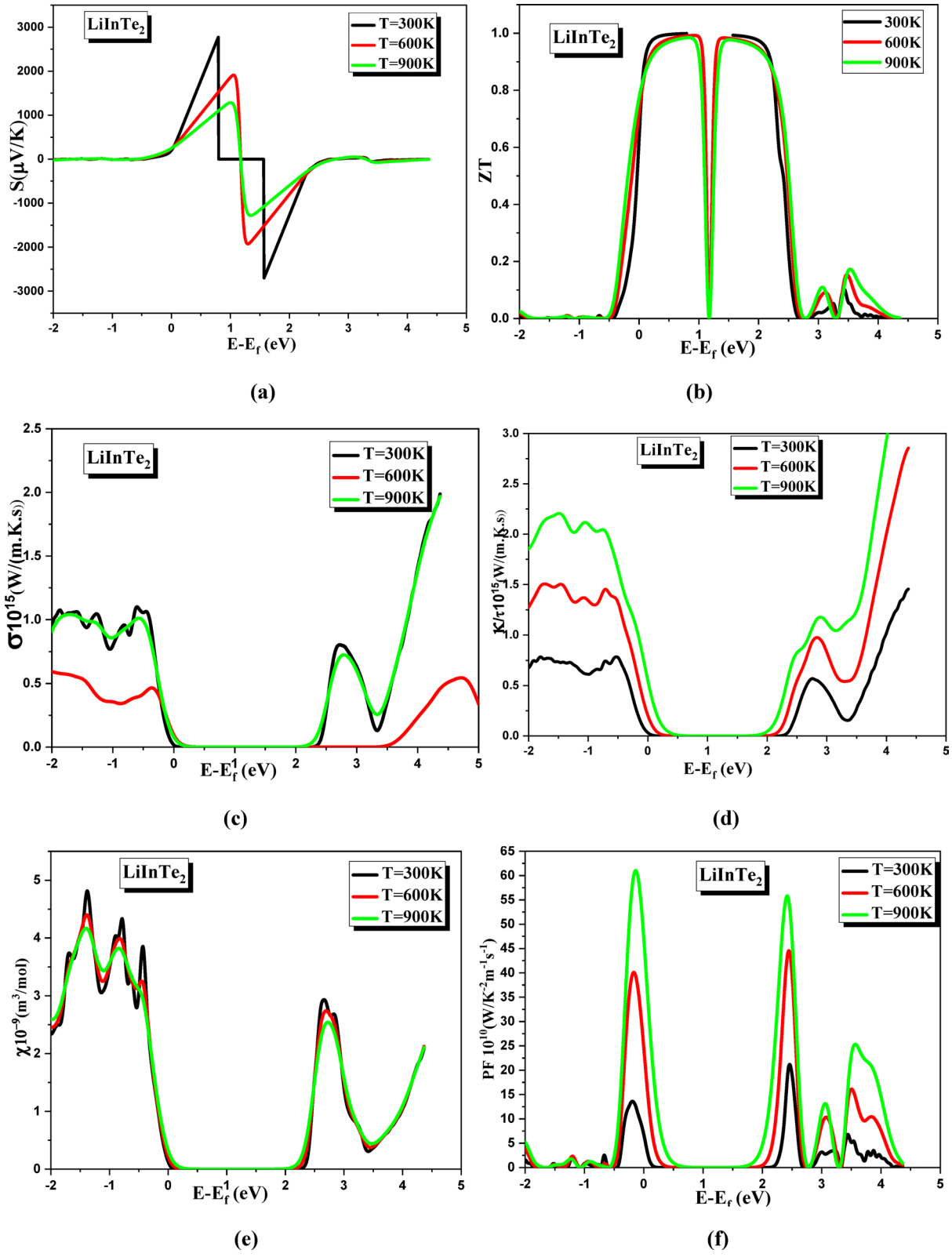

Fig. 12. The Seebeck coefficient (**a**), (**b**) the figure of merit ZT, (**c**) electronic thermal conductivity, (**d**) the thermal conductivity, (**e**) Magnetic susceptibility, (**f**) Power Factor within the mBJ-GGA approximation for $LiInTe_2$.

Data availability

Data Availability Statement: Data underlying the results presented in this paper are not publicly available at this time but may be obtained from the author (fatmimessaoud@yahoo.fr) upon reasonable request.

Received: 26 May 2025; Accepted: 28 July 2025
Published online: 30 July 2025

References

1. Isaenko, L. et al. Characterization of LiInS2 and LiInSe2 single crystals for nonlinear optical applications. MRS Online *Proc. Libr. OPL* 692, H9.7.1. (2001).
2. Ghebouli, M. A., Bouferrache, K., Alanazi, F. K., Ghebouli, B. & Fatmi, M. Computational insights into the stability, mechanical, optoelectronic, and thermoelectric characteristics investigation on Lead-Based double perovskites of (Cs2, K2, Rb2)PbCl6: promising candidates for optoelectronic applications. *Adv. Theory Simulations*. **8** (3), 2400938 (2025).
3. Min, J., Li, H. & Zhang, J. Volume modulation of nonlinear optical properties by cation substitution. *J. Phys. Chem. C*. **124**, 10679–10686 (2020).
4. Rahman, A., Li, S. & Zhang, Y. First-principles study of structural, elastic, electronic, optical and thermoelectric properties of liinse$_2$ chalcopyrite semiconductor. *Mater. Sci. Semiconduct. Process*. **139**, 106383 (2022).
5. Liu, W., Zheng, H., King, R. B. & Cotton, F. A. Recent advances in I-III-VI$_2$ chalcogenide semiconductors for photovoltaic applications. *Adv. Energy Mater.* **13** (8), 2203788 (2023).
6. Wang, J., Chen, L. & Snyder, G. J. Thermoelectric properties of ternary I-III-VI$_2$ chalcogenide semiconductors: A comparative study. *Energy Environ. Sci.* **15** (3), 967–985 (2022).
7. Kato, K., Miyamoto, K. & Pham, V. T. Wide-band-gap semiconductors for optoelectronic applications: current status and future prospects. *Appl. Phys. Reviews*. **8** (4), 041317 (2021).
8. Zhang, X., Xu, Z. & Chen, D. Lithium-containing multinary chalcogenides for non-linear optical applications in the mid-infrared region. *Adv. Opt. Mater.* **11** (12), 2202352 (2023).
9. Karki, V., Bhattarai, D. & Fujii, Y. Electronic and optical properties of liinte$_2$: A first-principles study. *Phys. B: Condens. Matter*. **628**, 413628 (2022).
10. Jones, R. O. Density functional theory: its origins, rise to prominence, and future. *Rev. Mod. Phys.* **93** (3), 035001 (2021).
11. Karaagac, H., Parlak, M. & Yilmaz, S. Investigation of structural, electronic and optical properties of liinse$_2$ for photovoltaic applications: an ab-initio study. *Sol. Energy Mater. Sol. Cells*. **247**, 112011 (2023).
12. Wang, K., Stevanović, V. & Bryce, D. A. High-throughput computational screening of thermoelectric properties in chalcogenide semiconductors. *Npj Comput. Mater.* **8** (1), 1–12 (2022).
13. Sharma, S., Kumar, R. & Patel, V. Defect-induced enhancement of thermoelectric properties in liins$_2$: A computational approach with experimental validation. *J. Mater. Chem. A*. **12** (3), 1452–1467 (2024).
14. Zhang, D., Liu, H. & Wang, T. Band gap engineering in liinx$_2$ (X = S, se, Te) compounds via strain and doping: First-principles insights. *Phys. Rev. Mater.* **7** (9), 095401 (2023).
15. Chen, Y., Gonzalez, J. & Martinez, A. Solution-processed liins$_2$ thin films for next-generation transparent photovoltaics. *Adv. Funct. Mater.* **34** (4), 2310647 (2024).
16. Zhou, K., Li, P. & Nguyen, M. Emergent ferroelectricity in chalcopyrite liinx$_2$ structures under pressure: A combined experimental and theoretical study. *Nat. Commun.* **14**, 4735 (2023).
17. Lee, J., Park, S. & Kim, T. First-principles analysis of structural phase transitions in liinte$_2$ under hydrostatic pressure. *Phys. Rev. B*. **108** (14), 144109 (2023).
18. Wang, H., Li, X. & Gao, Y. High-performance flexible photodetectors based on liins$_2$ nanocrystals with enhanced stability. *ACS Appl. Mater. Interfaces*. **16** (5), 6723–6735 (2024).
19. Mehta, N., Singh, R. & Kumar, A. Machine learning-guided discovery of novel LiInX$_2$-based materials for optoelectronic applications. *Npj Comput. Mater.* **9**, 112 (2023).
20. Ortiz-Ramos, D., Flores-Montaño, J. & Sánchez-Cruces, H. Comparative study of electronic and optical properties of liinx$_2$ (X = S, se, Te) compounds using hybrid functionals. *J. Appl. Phys.* **135** (2), 025701 (2024).
21. Lin, Y., Zhang, Z. & Wu, L. Electronic structure and optical properties of liinte$_2$: insights from GW calculations and experimental measurements. *Phys. Rev. B*. **107** (23), 235202 (2023).
22. Ahmad, S., Khan, Z. & Ali, S. Exploring the potential of liins$_2$ for high-efficiency all-solid-state batteries: A multiscale modeling approach. *Energy Storage Mater.* **57**, 102933 (2024).
23. Boudissa, R. et al. Prediction study of structural, electronic and optical properties of 4C16H10Br2O2 Bis (m-bromobenzoyl) methane crystals. *Biophys. Rep.* **37**, 101601 (2024).
24. Krache, L. et al. Phase Stability, Electronic, and Optical Properties in *Pcca*, *R3c*, and *Pm-3m* Phases of $BiGaO_3$ Perovskite, *Phys. Status Solidi B*, 2022, 259(10), 2200042. (2022).
25. Bouferrache, K. et al. Thermal, optoelectronic and thermoelectric properties of inorganic double perovskites semiconductors Cs2 (Sn, pt, Te) I6 for application as intermediate-band solar cells. *Solid State Commun.* **389**, 115522 (2024).
26. Benmakhlouf, A. et al. Structural elastic and thermodynamic properties of cubic CsCl type MgCa using Ab initio approach. *Sci. Rep.* **15** (1), 1–12 (2025).
27. Rahal, A. et al. Experimental investigation of structural and optical properties of Mn-doped ZnO thin, films deposited by pneumatic spray technique. *Sci. Rep.* **15** (1), 7086 (2025).
28. Born, M. & Huang, K. *Dynamical Theory of Crystal Lattices* (Oxford University Press, 1954).
29. Malki, S. et al. A First-Principles investigation on electronic structure and optical properties of tetragonal iron antimonide FeSb. *J. Supercond Nov Magn.* **35**, 1507–1516. https://doi.org/10.1007/s10948-022-06201-z (2022).
30. Siham Malki, I., Guesmi, Larbi, E. L., Farh, Z., Darhi, A. & Challioui FP-LAPW calculations of the structural, and optoelectronic properties of vanadium silicide compound for optoelectronic applications. *Solid State Commun.* **390**, 15611. https://doi.org/10.1016/j.ssc.2024.115611 (2024).
31. Malki, S. et al. Study of structural, electronic, optical and mechanical properties under pressure of GeTe for use in optoelectronic devices. *Emergent Mater.* **8**, 141–156. https://doi.org/10.1007/s42247-024-00911-x (2025).
32. Malki, S. et al. A First-Principles study of the effect of Spin–Orbit coupling on the optoelectronic and magnetic properties of manganese distannide. *J. Electron. Mater.* **54**, 2219–2228. https://doi.org/10.1007/s11664-024-11729-y (2025).

Acknowledgements

The authors extend their appreciation to Taif University, Saudi Arabia, for supporting this work through project number (TU-DSPP-2024-63).

Author contributions

Conceptualization: M.A. GhebouliData curation: K. BouferracheFormal analysis: S. Alomairy, Faisal Katib AlanaziMethodology: B. GhebouliValidation: M. Fatmi.

Declarations

Competing interests

The authors declare no competing interests.

Additional information

Correspondence and requests for materials should be addressed to M.F.

Reprints and permissions information is available at www.nature.com/reprints.

Publisher's note Springer Nature remains neutral with regard to jurisdictional claims in published maps and institutional affiliations.